On the Role of Polarimetric Decomposition and Speckle Filtering Methods for C-Band SAR Wetland Classification Purposes

Monika Gierszewska and Tomasz Berezowski, *Member, IEEE*

***Abstract*—Previous wetlands studies have thoroughly verified the usefulness of data from synthetic aperture radar (SAR) sensors in various acquisition modes. However, the effect of the processing parameters in wetland classification remains poorly explored. In this study, we investigated the influence of speckle filters and decomposition methods with different combinations of filter and decomposition windows sizes on classification accuracy. We used a C-band Radarsat 2 image acquired over a wetland located in northeast Poland. We processed the SAR data using various speckle filters: boxcar, intensity-driven adaptive-neighborhood (IDAN), improved Lee sigma, refined Lee (in 5×5 to 11×11 pixel window sizes), and a nonlocal NL-SAR. Next, we processed the nonfiltered and filtered data using nine polarimetric decompositions, also in 5×5 to 11×11 pixel window sizes. The extracted polarimetric features were applied as an input dataset in the random forest classification model in single- and multidecomposition scenarios. In the single-decomposition scenario, the Cloude–Pottier decomposition produced the highest (72%) and the Touzi decomposition achieved the lowest (38%) accuracy. The IDAN filter with an 11×11 filter window and a 9×9 decomposition window had the highest, and the nonfiltered data with a 5×5 decomposition window had the lowest accuracy in the multidecomposition scenario. The most important features were the alpha parameter from the Cloude–Pottier decomposition, the polarimetric contribution of the Shannon entropy, and the volume backscattering components. The results stress the importance of appropriate processing parameters in the SAR data classification workflow, and the study guides in selecting the most suitable combination of radar image processing parameters for wetland classification.**

***Index Terms*—Classification, polarimetric decomposition, synthetic aperture radar (SAR), speckle filtering, wetlands.**

I. Introduction

In RECENT years, many studies focused on the application of different synthetic aperture radar (SAR) data in wetlands mapping using various acquisition setups. The studies showed an impact on the classification accuracy of the SAR band, polarization mode, multiple acquisition dates [1]–[5], and incidence angles of the beam [6], [7]. At the same time, the selection of the polarimetric processing parameters of the SAR images was rarely justified, while only several studies demonstrated that these parameters influence the workflow.

The first parameter which affects the polarimetric decomposition product is the speckle filtering method [8], [9]. It was shown that the application of the speckle filtering improved the classification accuracy [10], and that the improvement depends on both the speckle filtering algorithm and the filter window size [11]–[14].

In speckle filtering of full polarimetric images in wetland areas, the most often used methods were the refined Lee filter [4], [15] with a 5×5 [2] or 7×7 window [5], the boxcar filter with a 5×5 window [7], [16], [17], and the improved Lee sigma filter with a 3×3 [3] or 5×5 window [1]. These filters reduce speckle based on the local window, while a recent approach is to use nonlocal filters, which were useful in coastal studies [18], [19] and floodplain boundary preservation [20]. The nonlocal filters often have different parametrization than local filters and use an adaptive approach instead of a defined filtering window.

Most of the wetland studies processed SAR data with one method of speckle filtering without comparison with others and determining the impact of the filtering method on the classification results. A study conducted in Indian coastal wetlands using ERS-1 SAR data showed that the 5×5 window size for the Lee filter was superior in suppressing the noise and preserving the image contrast when compared to 3×3 and 7×7 windows [21]. Research that is more comprehensive compared the application of the boxcar, Frost, Gamma map, Lee, Lee sigma, and median filters for single-channel SAR images with 3×3 and 5×5 kernel sizes in mapping flooded areas [22]. Similarly, a study conducted in Canadian boreal wetlands compared five different speckle filters [23]. These studies evaluated the performance of different filters without focusing on a wide range of filtering window sizes. Unfortunately, studies showing the effect of the multiple polarimetric speckle filters with different (small and large) filter window sizes on classification results are lacking.

The second important parameter in the decomposition calculation workflow is the decomposition window size, which determines the area for decomposition input averaging. According to our literature review, authors rarely test the effect of the decomposition window size in SAR polarimetric studies. The lack of interest in this parameter may be due to the expectation that averaging polarimetric data for the decomposition may have a similar effect as averaging during the speckle-filtering step.

Manuscript received December 30, 2021; revised March 3, 2022; accepted March 22, 2022. Date of publication March 28, 2022; date of current version April 20, 2022. This work was supported by the National Science Centre, Poland under Grant 2017/26/D/ST10/00665. *(Corresponding author: Tomasz Berezowski.)*

The authors are with the Faculty of Electronics, Telecommunication and Informatics, Gdansk University of Technology, 80-233 Gdansk, Poland (e-mail: monika.gierszewska1@pg.edu.pl; tomberez@eti.pg.edu.pl).

Digital Object Identifier 10.1109/JSTARS.2022.3162641

However, it was shown that the decomposition window size influences the classification results for the city of Prague [14]. Therefore, it is interesting to test this relationship for other speckle filtering methods including with the decomposition window size smaller than the filter window size.

Finally, the key step in SAR polarimetric workflow is the polarimetric decomposition, which makes it possible to decompose a complex coherency or covariance matrix into real parameters or components, which are used as a classification input. Many studies have confirmed the applicability of polarimetric SAR data in wetland classification. The Shannon entropy parameter provided the best classification results and was the most discriminating SAR feature regardless of the polarization mode and frequency [5], [15], [24]. Several other studies showed that the Cloude–Pottier decomposition, which also decomposes Shannon entropy, was an important classification feature [6], [25]. On the other hand, the helix scattering component from the Yamaguchi decomposition was useful in detecting the flooded vegetation class in certain configurations [4]. Another study showed that the decompositions based on the scattering model (Freeman–Durden, Yamaguchi) and the van Zyl decomposition classified Amazon wetlands better than eigenvector-based decompositions (Touzi, Cloude–Pottier) [2]. For the classification of boreal wetlands, the Yamaguchi and Touzi decompositions were more useful than the Cloude–Pottier and Freeman–Durden decompositions [1]. In addition, the phase parameter from the Touzi decomposition was able to distinguish between fen and bog wetlands in Canada, which was not possible using Cloude–Pottier decomposition parameters and backscatter coefficients [26]. To summarize the aforementioned studies, various polarimetric decomposition methods in different study areas were successfully used, however, there is no consistent conclusion on which SAR features are the most useful for wetland classification.

In this study, we investigated the effect of preprocessing parameters, such as speckle filters and polarimetric decompositions with various combinations of filter and decomposition window sizes on wetland classification accuracy. We processed a Radarsat 2 image with boxcar, intensity-driven adaptive-neighborhood (IDAN), refined Lee, and improved Lee sigma filters using four different filter window sizes (5×5, 7×7, 9×9, and 11×11) as well as with a nonlocal-SAR (NL-SAR) filter. Then from the nonfiltered and filtered images, we extracted 30 polarimetric features from nine decomposition methods (Cloude, Cloude–Pottier, Freeman–Durden, generalized Freeman–Durden, Pauli, Sinclair, Touzi, van Zyl, and Yamaguchi). In the decomposition step, we also used four different decomposition window sizes (5×5, 7×7, 9×9, and 11×11). The calculated polarimetric parameters, together with the topographic slope, were used as an input in a random forest supervised classification model. We used three scenarios of input data combinations: 1) single-decomposition, 2) multidecomposition with the same speckle filter, and 3) with all (decomposition and filtering methods) data. Finally, we discuss the parameters used to identify the interrelations of the parameters and to assist in selecting the optimal workflow for wetlands classification.

An important factor in our study was the spatial resolution of the radar image because the recommended filter and decomposition windows may be useful only for the processing of data with a similar spatial resolution. In addition, the frequency of the SAR data influences the ability to discriminate wetland classes, so our results refer only to C-band SAR images.

II. Methods

A. Data Acquisition and Processing

A Radarsat-2 C-band, single look complex (SLC) image in fine quad polarization (FQ3) mode was acquired for the study area on the 30th of March 2019 [Fig. 1(b)]. In FQ3 mode, the incidence angle is approx. 21° and the spatial resolution of the image is approximately 10.2×6 m (range × azimuth). The SAR image was processed using the python snappy package, which is an extension of the ESA SNAP 8.0 remote sensing processing software. The image processing consisted of radiometric calibration, polarimetric speckle filtering, polarimetric decomposition, and range-Doppler terrain correction. The DEM used in the terrain correction was shuttle radar topography mission (SRTM) 1 Arc-Second Global. We also produced a nonfiltered dataset where instead of the speckle-removal step the polarimetric coherency matrix was calculated. After the preprocessing and classification, the spatial resolution was 12.7×7.6 m. The nonsquare pixel size was due to projecting the raster data in geographical coordinates into a Cartesian coordinate reference system.

We implemented the speckle filtering with five different filters: 1) boxcar, 2) IDAN, 3) improved Lee sigma, 4) refined Lee, and 5) nonlocal NL-SAR. The boxcar filter is a simple averaging filter that replaces the center pixel by the mean value of all pixels in a sliding window. It presents the best filtering performance over homogeneous areas [27]. The refined Lee filter selects a directional window from eight edge-aligned windows, based on determining the most homogeneous part of the sliding window. The minimum mean square algorithm is applied for pixels in the nonedge area in the edge-aligned window [28]. The IDAN filter does not select pixels from homogeneous areas as a constant sliding window. Instead, it uses region-growing techniques that select as many pixels as possible, all following the same statistical population as the pixel of interest. The pixel is filtered with the minimum mean square error (MMSE) filter computed using all selected pixels [29]. The improved Lee sigma filter first detects pixels that represent strong scattering targets, which remain unfiltered. The filter then selects pixels within the sigma range from a window and applies MMSE to the coherency matrix [30]. The nonlocal filter is a novel paradigm for the preservation of the image's fine structure, details, and texture in image denoising. It smooths images by deriving data-driven weights from the similarity between small image patches. The NL-SAR algorithm defines the nonlocal neighborhoods based on pixel similarity evaluated by multichannel comparison of patches. Several nonlocal estimations are performed, and the best one is locally selected to form a single restored image with good preservation of radar structures [31].

In this study, we used filter windows with the following sizes: 5×5, 7×7, 9×9, and 11×11 pixels. The number of looks parameter was 1 for IDAN, refined Lee, improved Lee sigma, and NL-SAR filters. In the improved Lee sigma filter, the sigma

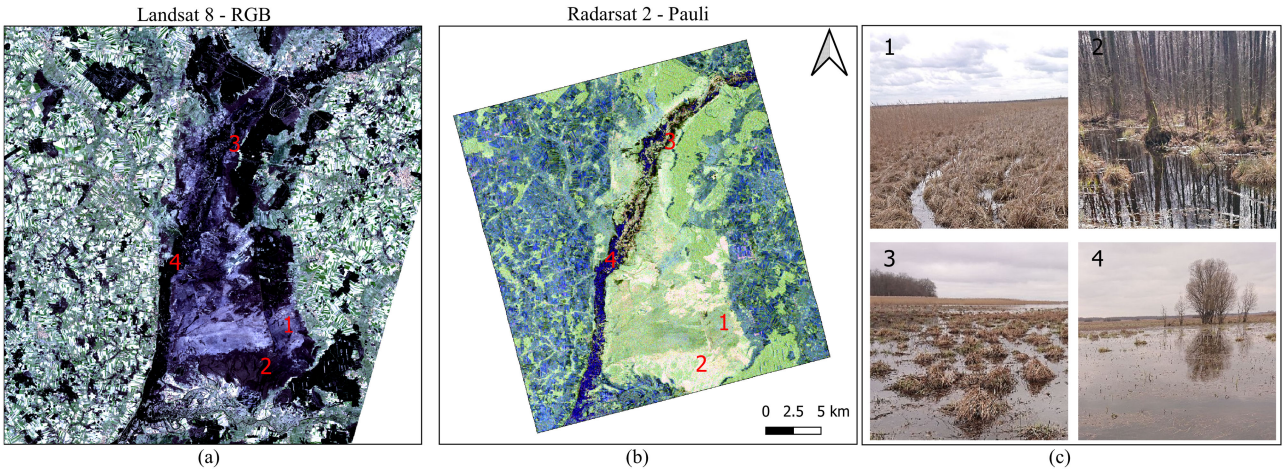

Fig. 1. (a) True color Landsat 8 image of the study area acquired on 2nd April 2019, i.e., three days after the (b) Radarsat-2 image used in this study. The Radarsat 2 image is presented in the Pauli color composition: red – double, green – volume, and blue – surface. Panels 1–4 (c) show different vegetation types and flooding conditions present in the study area.

value was 0.9 and the target window size was 3×3. In the IDAN filter, the adaptive neighborhood size parameter was 25, 50, 80, and 120 pixels, which correspond to the number of pixels in the filter windows with sizes from 5×5 to 11×11 used for the remaining filters (except the NL-SAR). In the NL-SAR filter, the search window radius parameter was set to 1 to 12 pixels range, the patch size with the half-width parameter was set to 0 to 5 pixels range, and the patch similarity criterion function was the generalized likelihood ratio. Note that the NL-SAR parameter values correspond to the filter window sizes applied in the remaining filtering methods. We also used nonfiltered data in form of a coherency matrix, since some SAR methods are based on speckled data [32].

In the polarimetric decomposition steps, we used coherent decompositions using the scattering matrix, and model-based and eigenvector-based decompositions using the covariance matrix or coherency matrix. Coherent decompositions express the scattering matrix as a combination of scattering responses of simpler objects, known as canonical objects [28]. The model-based decompositions are based on the assumption that the reflection from an object can be modeled as the sum of the different types of scattering: surface (single, or odd), double (even), and volume [33], and added in Yamaguchi decomposition helix [34]. Eigenvector-based decomposition uses eigenvector and eigenvalues analysis of the coherency matrix. The method assumes that the presence of a scattering mechanism is indicated by a nonzero eigenvalue and when all eigenvalues have equal values, the scattering is random [28].

We decomposed the SAR image with the following coherent decompositions: Sinclair, and Pauli; model-based decompositions: Freeman–Durden, generalized Freeman–Durden, and Yamaguchi; eigenvector-based decompositions: Cloude, Cloude–Pottier, Touzi, and van Zyl. We also calculated two Shannon entropy contributions related to intensity and polarimetry [35], whose sum corresponds to the entropy component in the Cloude–Pottier decomposition. We calculated the eigenvector- and model-based decompositions in a decomposition window with the following sizes: 5×5, 7×7, 9×9, and 11×11 pixels. The various window sizes were not used in the Pauli and Sinclair decompositions as these methods decomposed the coherency matrix in each pixel without averaging (i.e., 1×1 window) in the SNAP software.

The aforementioned methods extend our preliminary study design, which investigated only two speckle-filtering methods in one decomposition and filtration window size [36], to give a broader look at the effect of polarimetric processing parameters on the classification accuracy and the individual polarimetric features' importance.

B. Study Area

The study was conducted in the lower Biebrza basin (approx. 220 km^2), located in northeastern Poland (53.3°N, 22.6°E; Fig. 1). The basin is composed mostly of fen wetlands, which are flooded yearly in spring due to river flooding and snowmelt, rainfall, and groundwater discharge in areas located further away from the river [37]. The wetlands have been subjected to only minor anthropogenic influence over the last few centuries and are currently protected by National Park status in Poland and by the Ramsar and Natura 2000 acts internationally. Notably, the lower Biebrza basin is considered a reference site for comparable fen and floodplain European wetlands [38]. The majority of the terrain is overgrown by the low vegetation, such as sedges, reeds, scrubs, meadows, and their mosaics; within the wetlands, some patches of alder and birch tree are present, as well as a major alder forest located in the southern part (Fig. 1).

C. Field Measurements

Measurements of the flooding extent and vegetation types in different locations of the study area were carried out on the 27–29th of March 2019. We used a handheld GPS receiver with a horizontal accuracy of approx. 2 m. The vegetation was dry and leafless except for the coniferous trees in the upland. Such conditions are typical for spring floods in European temperate

zone wetlands. We collected 113 points and refined them locally with additional 413 points based on an analysis of a 1×1-m LiDAR-based digital elevation model developed in 2015, a 15-cm orthophoto map, and a Landsat 8 satellite image [Fig. 1(a)] acquired a week after the field measurements. We distinguished six land cover classes that reflected well the flooding conditions during the sampling, labeled as dense vegetation (DV), not flooded terrain (NFT), soil (SL), open water (OW), flooded vegetation below 10-cm high (FVB), and flooded vegetation above 10-cm high (FVA). The discrimination between the FVA and FVB classes was conducted based on approximated vegetation height above the water. These classes included such vegetation as meadows, grasslands, as well as deeply flooded sedges, and reeds [Fig. 1(c): 3, 4]. In the DV class, we included both flooded and not flooded vegetation that was too high and too dense for the C-band SAR beam to scatter from the water surface beneath the vegetation. The vegetation types in the DV class were high reeds, dense sedges with tussocks, and forests [Fig. 1(c): 1, 2]. The OW class was mostly present in the proximity (<2 km) of the river, where the flooding was the deepest and no vegetation was emerging. The NFT and SL classes were only present in the upland and were covered mostly by agriculture in various development states.

D. Image Classification

After processing the SAR image, we produced (for each decomposition and each decomposition window size) 18 sets of data including five speckle filtering methods boxcar, IDAN, improved Lee sigma, refined Lee (in four filter windows), and NL-SAR (in only one filtering parameter set), as well as nonfiltered coherency matrix. Further, the processed dataset and the topographic slope raster were sampled in the 526 field measurement locations and randomly split into training and validation subsets (50/50%). We used the training subsets as the input to the random forest machine learning classification model.

The random forest algorithm is an ensemble classifier based on decision trees. This algorithm is popular in remote sensing studies due to the accuracy of its classifications and robustness [39]. The samples and variables are selected randomly from the input dataset and used to train the trees. The final class label is decided by voting using the class assignment by all trees (in this research 1000) [40].

We ran the random forest classification for each combination of processing parameters in the following three scenarios (Fig. 2).

1) Each decomposition product was used separately as the model input.
2) All decomposition products with the same speckle filtering method were used as the model input.
3) All decomposition products with the same combination of filter and decomposition window size were used together as the model input.

Our initial tests showed that classification results were erroneous in the area of the high-slope valley margin, situated nearly perpendicular to the Radarsat-2 azimuth axis. The errors were due to shadow and overlay radar distortions caused by that landform. We were not able to correct this region using the SAR terrain correction methods. These regions produced erroneous classification results in each classification, which was undesired in this study. Therefore, we introduced slope as a classification feature in each classification model. The slope allowed the random forest algorithm to learn to distinguish flat wetland surfaces (OW, FVB, FVA, DV classes) from sloppy landforms affected by radar distortions (mostly in NFT, SL, DV classes). Effectively, the classification accuracy improved by about 1–2% in our preliminary study (not discussed here).

E. Validation

To validate the random forest classifications from the different scenarios and variants, we calculated the overall accuracy [%]

$$z = 100\frac{k}{n} \tag{1}$$

where k is the number of correctly classified pixels, and n is the number of all pixels in the validation subset. For each class, we calculated the user accuracy (precision), which is a ratio of correctly classified pixels in a class to the total number of pixels that were classified in that class, and the producer accuracy (sensitivity), which is a ratio of the number of correct pixels in a class by the total number of pixels in that class in reference data.

We performed the Kruskal–Wallis [41] and Dunn [42] tests to determine whether using different speckle filtering and decomposition methods lead to significantly different classification accuracy. The Kruskal–Wallis is a nonparametric rank test, which shows if two or more groups have equal medians without pointing out the between-group differences. To point out exactly which groups have a different median, we performed the Dunn post-hoc test with the Bonferroni correction of the p-values. In this study, the Kruskal–Wallis and Dunn tests are used to show whether the accuracy, (1), of multiple classification models grouped by a given filtering or decomposition method is significantly different from another group. Hence, this approach shows if there is a pattern in classification accuracy resulting from the polarimetric methods applied in processing of the SAR data.

F. Ranking the Importance of SAR Features

For each classification model in scenario 2, we identified the most important parameters or components from each polarimetric decomposition. The random forest algorithm provides an assessment of the importance of input features during the classification process. To evaluate the importance of each predictor, the mean decrease in the Gini index is calculated based on the Gini impurity metric. The Gini impurity shows how much a predictor reduces the impurity in a particular class [39]. Finally, predictor importance is calculated as the average of decreasing the Gini impurity across all trees in the forest [40]. To achieve reliable comparison, we ranked the predictors' importance only for models from scenario 2, where each model used the same predictors set differentiated only by a speckle filtering method.

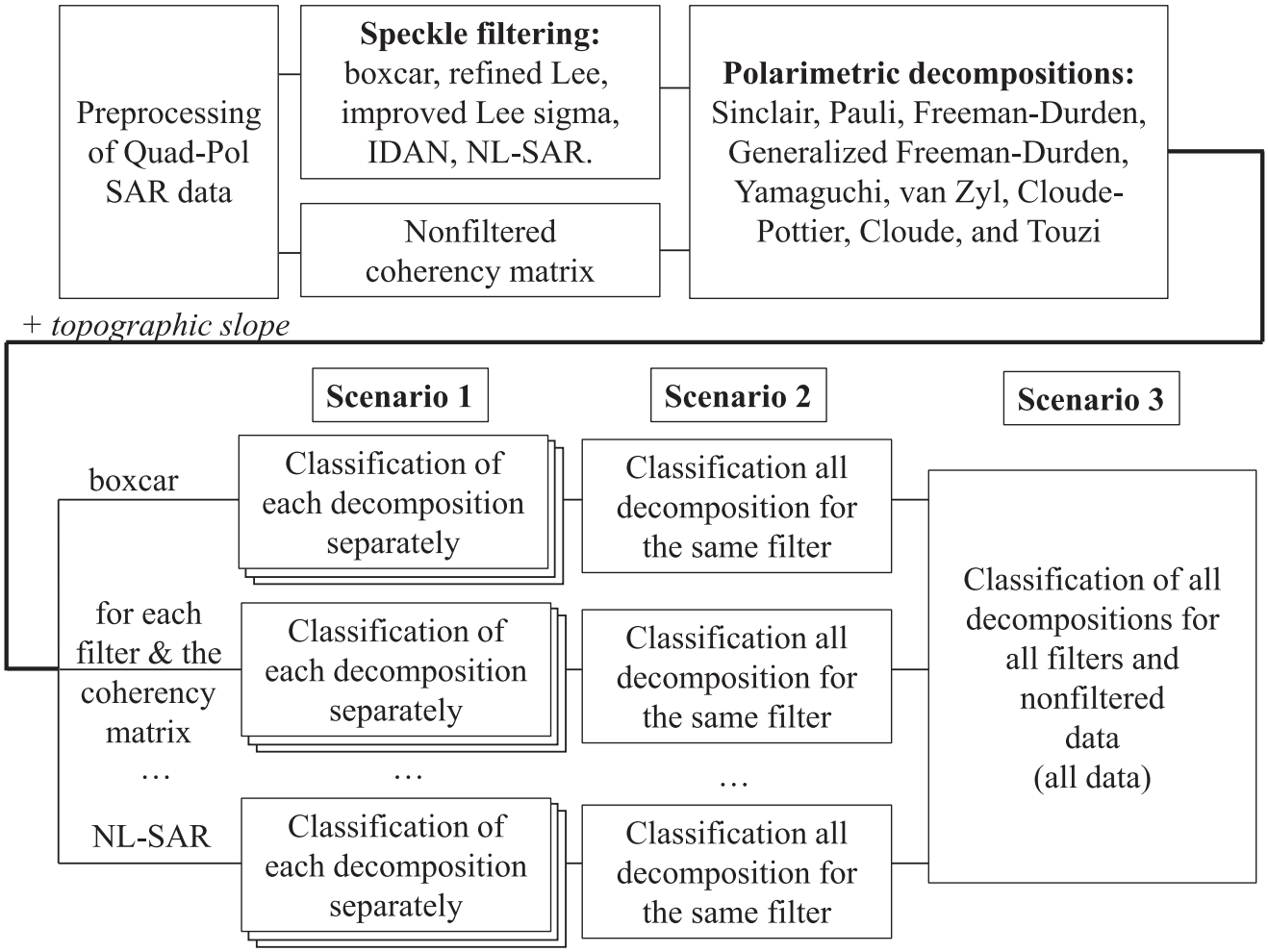

Fig. 2. Flowchart describing the classification scenarios used in this study. Each decomposition and speckle filter (except NL-SAR) was conducted in multiple window sizes, but this dimension of analysis is removed from the figure for clarity.

G. Sensitivity of Accuracy to Processing Window Size

To quantify the effect of increasing the decomposition and filter window sizes on the classification accuracy, we used a sensitivity approach. Here, we define the sensitivity as the average slope of accuracy for subsequently increasing decomposition or filter window sizes. This approach is analogous to other methods used for model parameters sensitivity analysis. The filter windows sensitivity [%] is

$$s_f = \frac{\sum_{i=1}^{n}\sum_{j=2}^{m}\frac{z_{i,j}-z_{i,j-1}}{f_{i,j}-f_{i,j-1}}}{n(m-1)} \tag{2}$$

and the decomposition window sensitivity [%] is

$$s_d = \frac{\sum_{i=2}^{n}\sum_{j=1}^{m}\frac{z_{i,j}-z_{i-1,j}}{d_{i,j}-d_{i-1,j}}}{(n-1)m} \tag{3}$$

where z is accuracy [%] (1); f and d are half of the window size (2.5, 3.5, 4.5, or 5.5) of the filter and decomposition windows, respectively; and i and j are variant numbers out of n and m total numbers of variants of the filter and decomposition windows, respectively.

III. Results

A. Scenario 1

In scenario 1, we performed in total 540 classifications of single decompositions with different processing parameters combinations (Fig. 3). The median accuracy for the Cloude–Pottier decomposition models was the highest (66.4%) and was significantly different from other decompositions except for the Pauli (Fig. 3 and Table II). The highest accuracy (72.1%) was for a model using the Cloude–Pottier decomposition with the IDAN filter, 9×9 speckle filtering window, and the 11×11 decomposition window (Fig. 7, Table I). The user accuracy for this classification was the highest for the DV class (83%) and the lowest for the NFT class (62%), and the producer accuracy was the highest for the DV class (87%) and the lowest for the SL class (64%) (Table I).

The lowest accuracy (37.7%) was obtained for the Touzi decomposition with a nonfiltered coherency matrix and the 7×7 decomposition window size. The median accuracy of the models using Touzi decomposition (50.6%) was significantly different from other decompositions except for the Cloude (Table II). The user accuracy for this classification was the highest for the FVB

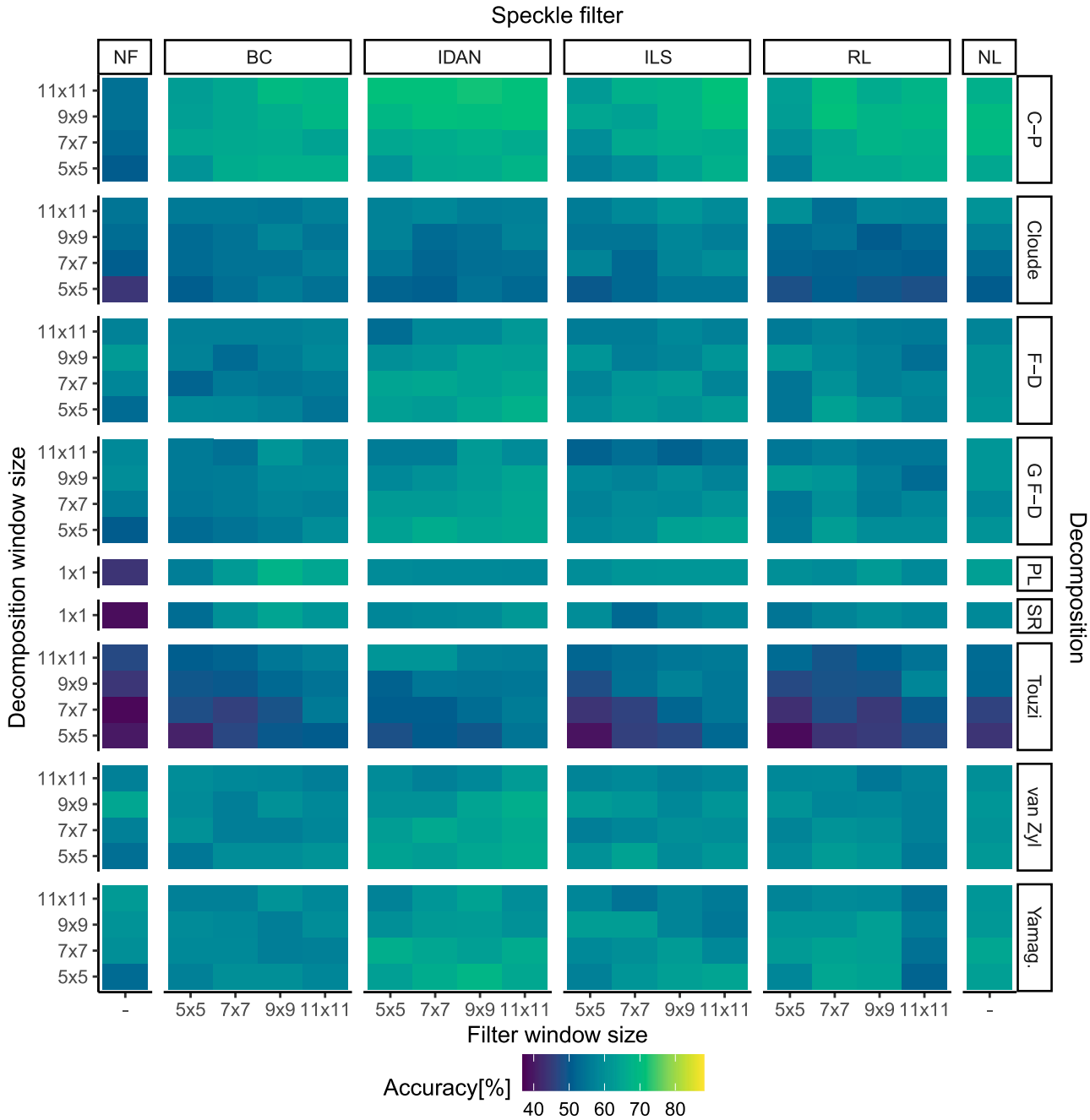

Fig. 3. Accuracy of random forest classification models in scenario 1. Panels are varied by the filter used (columns) and decomposition calculated (rows). Within each panel, accuracy is shown per filter window size (panel columns) and decomposition window size (panel rows). Filter abbreviations: nonfiltered coherency matrix (NF), boxcar (BC), intensity-driven adaptive-neighborhood (IDAN), improved Lee sigma (ILS), refined Lee (RL), and NL-SAR (NL). Decomposition abbreviations: Sinclair (SR), Pauli (PL), Freeman–Durden (F-D), generalized Freeman–Durden (G F-D), Yamaguchi (Yamag.), and Cloude–Pottier (C-P). The accuracy color scale is the same in Figs. 3, 4, and 6.

class (48%) and the lowest for the NFT class (24%), and the producer accuracy was the highest for the DV class (51%) and the lowest for the NFT class (24%) (Table I).

In the scope of the filtering method used, the median of the classification accuracies from scenario 1 was the highest for datasets processed with IDAN (61.6%). The Dunn test showed that the IDAN median accuracy was significantly different from the median accuracies of the other speckle filters except for the NL-SAR filter whose median accuracy was 60.7% (Table III). The lowest median accuracy was for the nonfiltered coherency matrix (54%) which was not significantly different from the median accuracy of the boxcar (56.8%), and refined Lee (57.6%) filters.

B. *Scenario 2*

In scenario 2, the classification of all decompositions with the same speckle filter was performed in 72 different processing combinations (Fig. 4). The highest accuracy (84%) was obtained for images processed with the IDAN filter with the 11×11 filter

TABLE I
CONFUSION MATRICES FOR THE LOWEST (LEFT) AND HIGHEST (RIGHT) ACCURACY VARIANTS FOR SCENARIOS 1 (A, B), 2 (C, D), AND 3 (E, F)

Scenario 1

(a) nonfiltered Touzi in 7x7 window

Classes	DV	NFT	OW	SL	FVB	FVA	UA [%]
DV	20	9	4	0	3	16	38
NFT	6	11	5	4	14	6	24
OW	3	4	20	13	3	1	45
SL	0	9	14	18	3	2	39
FVB	0	6	2	7	16	2	48
FVA	10	6	4	2	5	14	34
PA[%]	51	24	41	41	36	34	z =37.8%

(b) Cloude-Pottier in 11x11 window and IDAN in 9x9 window

Classes	DV	NFT	OW	SL	FVB	FVA	UA [%]
DV	34	1	0	0	0	6	83
NFT	2	31	3	5	3	6	62
OW	0	0	36	8	2	0	78
SL	0	2	6	28	5	1	67
FVB	1	7	4	2	33	1	69
FVA	2	4	0	1	1	27	77
PA[%]	87	69	73	64	75	66	z =72.1%

Scenario 2

(c) All nonfiltered decompositions in 5x5 window

Classes	DV	NFT	OW	SL	FVB	FVA	UA [%]
DV	30	1	0	0	1	10	71
NFT	4	28	3	2	3	2	67
OW	0	1	33	7	1	1	77
SL	0	5	6	28	3	0	67
FVB	0	3	6	7	29	3	60
FVA	5	7	1	0	7	25	56
PA[%]	77	62	67	64	66	61	z= 66.0%

(d) All decompositions in 9x9 window and IDAN in 11x11 window

Classes	DV	NFT	OW	SL	FVB	FVA	UA [%]
DV	38	1	0	0	0	3	90
NFT	1	42	3	3	1	0	84
OW	0	0	38	4	1	0	88
SL	0	1	5	34	3	1	77
FVB	0	1	3	3	34	2	79
FVA	0	0	0	0	5	35	88
PA[%]	97	93	78	77	77	85	z= 84.4%

Scenario 3

(e) All filters and decompositions in the 5x5 window

Classes	DV	NFT	OW	SL	FVB	FVA	UA [%]
DV	38	1	0	0	0	6	84
NFT	0	35	1	3	0	3	83
OW	0	0	34	7	0	0	83
SL	0	3	5	30	2	0	75
FVB	0	3	9	4	35	3	65
FVA	1	3	0	0	7	29	73
PA [%]	97	78	69	68	80	71	z= 76.7%

(f) All filters and decompositions in the 11x11 window

Classes	DV	NFT	OW	SL	FVB	FVA	UA [%]
DV	37	1	0	0	0	1	95
NFT	0	39	1	2	0	0	93
OW	0	0	40	2	1	0	93
SL	0	1	3	35	3	0	83
FVB	0	1	5	5	37	2	74
FVA	2	3	0	0	3	38	83
PA [%]	95	87	82	80	84	93	z= 86.3%

z – overall accuracy (1), UA – user accuracy, PA – producer accuracy. Classes abbreviations: dense vegetation (DV), not flooded terrain (NFT), soil (SL), open water (OW), flooded vegetation below 10-cm high (FVB), and flooded vegetation above 10-cm high (FVA).

TABLE II
PAIRWISE DUNN TEST FOR MEDIAN ACCURACY DIFFERENCE BETWEEN GROUPS DEFINED BY POLARIMETRIC DECOMPOSITIONS IN SCENARIO 1

	Median accuracy [%]	Dunn test on median difference p-value							
		C-P	Cloude	F-D	GF-D	PL	SR	Touzi	van Zyl
C-P	66.4	-	-	-	-	-	-	-	-
Cloude	54.6	<0.001	-	-	-	-	-	-	-
F-D	58.2	<0.001	<0.001	-	-	-	-	-	-
GF-D	58.4	<0.001	<0.001	1.000	-	-	-	-	-
PL	59.7	0.054	<0.001	1.000	1.000	-	-	-	-
SR	58.4	<0.001	0.073	1.000	1.000	1.000	-	-	-
Touzi	50.6	<0.001	0.261	<0.001	<0.001	<0.001	<0.001	-	-
van Zyl	59.5	<0.001	<0.001	1.000	1.000	1.000	1.000	<0.001	-
Yamag.	59.9	<0.001	<0.001	1.000	0.482	1.000	1.000	<0.001	1.000

A significant difference is indicated by a p-value < 0.05. Decomposition abbreviations: Sinclair (SR), Pauli (PL), Freeman–Durden (F-D), generalized Freeman–Durden (G F-D), Yamaguchi (Yamag.), and Cloude–Pottier (C-P).

TABLE III
PAIRWISE DUNN TEST FOR MEDIAN ACCURACY DIFFERENCE BETWEEN GROUPS DEFINED BY SPECKLE FILTERS IN SCENARIO 1

	Median accuracy [%]	Dunn test on median difference p-value				
		NF	BC	IDAN	ILS	RL
NF	54.0	-	-	-	-	-
BC	56.8	0.065	-	-	-	-
IDAN	61.6	<0.001	<0.001	-	-	-
ILS	58.4	0.002	0.651	0.005	-	-
RL	57.6	0.039	1.000	<0.001	1.000	-
NL	60.7	<0.001	0.070	1.000	0.974	0.114

A significant difference is indicated by a p-value < 0.05. Filter abbreviations: nonfiltered coherency matrix (NF), boxcar (BC), intensity-driven adaptive-neighborhood (IDAN), improved Lee sigma (ILS), refined Lee (RL), and NL-SAR (NL).

and 9×9 decomposition window sizes (Figs. 4 and 7, Table I). The user accuracy for this classification was the highest for the DV class (90%) and the lowest for the SL class (77%), and the producer accuracy was the highest for the DV class (97%) and the lowest for the SL and FVB classes (77%) (Table I).

The classification model based on a 5×5 decomposition of nonfiltered coherency matrix had the lowest accuracy (66%). The user accuracy for this classification was the highest for the OW class (77%) and the lowest for the FVA class (56%), and the producer accuracy was the highest for the DV class (77%) and the lowest for the FVA class (61%). In 56% of the analyzed combinations of processing window sizes, the classification of images processed with the IDAN filter provided the highest accuracies. The lowest accuracies were produced by the decompositions of the nonfiltered coherency matrix (69% of variants). The highest average accuracy was 79% for four variants: 11–11, 11–9, 7–11, and 9–11 (filter-decomposition window size). The lowest accuracy (72%) was obtained by the 5×5 filter and 5×5 decomposition windows.

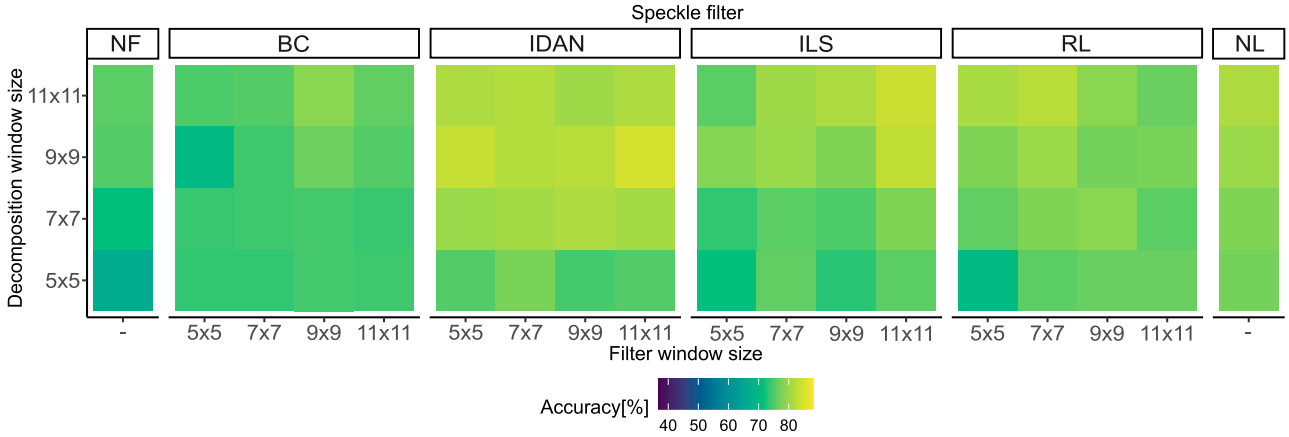

Fig. 4. Accuracy of random forest classification models in scenario 2. Panels are varied by filters used (columns). Within each panel, accuracy is shown per filter window size (panel columns) and decomposition window size (panel row). Filter abbreviations: nonfiltered coherency matrix (NF), boxcar (BC), intensity-driven adaptive-neighborhood (IDAN), improved Lee sigma (ILS), refined Lee (RL), and NL-SAR (NL). The accuracy color scale is the same in Figs. 3, 4, and 6.

The sensitivity of accuracy to the decomposition window size was the highest for the nonfiltered variant where the increase of decomposition window increased the accuracy by $s_d = 3.18\%$ on average. The second highest sensitivity was for improved Lee sigma ($s_d = 2.07\%$), followed by IDAN ($s_d = 1.84\%$), refined Lee ($s_d = 1.65\%$), NL-SAR ($s_d = 1.40\%$), and boxcar ($s_d = 0.80\%$) scenario 2 variants. The sensitivity of accuracy to filter window size was the highest for the improved Lee sigma variant, where the increase of filtering window size increased the accuracy by $s_f = 1.78\%$ on average. The second highest sensitivity was for boxcar ($s_f = 0.64\%$), followed by IDAN ($s_f = 0.16\%$), and refined Lee ($s_f = 0.10\%$) scenario 2 variants; nonfiltered and NL-SAR variants were not evaluated because they did not have the filtering window size parameter.

The alpha parameter from the Cloude–Pottier decomposition was the most important predictor for wetlands classification in our case study (except for the topographic slope, which is not a polarimetric feature; Fig. 5). Other important predictors were the polarimetric contribution of the Shannon entropy, volume components (except the Cloude decomposition). The double scattering component from Pauli decomposition and the alpha parameter from Touzi decomposition were moderately important. The least important predictors were the double (except the Cloude and Pauli decompositions) and helix scattering components.

C. Scenario 3

In this scenario, we performed the classification of all polarimetric decompositions and processed with five various speckle filters in 16 different combinations of processing windows sizes. Thus, one variant from this scenario includes data from 54 variants from scenario 1 or six variants from scenario 2. The highest overall accuracy (86.3%) was achieved by images processed with an 11×11 filter and 11×11 decomposition window sizes (Figs. 6 and 7, Table I). The user accuracy for this classification was the highest for the DV class (95%) and the lowest for the FVB class (74%), and the producer accuracy was the highest for the DV class (95%) and the lowest for the FVB class (80%) (Table I). The variant with 5×5 speckle filtering and 5×5 decomposition window sizes produced the lowest accuracy (76.7%). The user accuracy for this classification was the highest for the DV class (84%) and the lowest for the FVB class (65%), and the producer accuracy was the highest for the DV class (97%) and the lowest for the SL class (68%). The median accuracy was 81%.

In this scenario, the accuracy was slightly more sensitive to the decomposition window ($s_d = 1.53\%$) than the filter window ($s_f = 1.30\%$) sizes.

The classified map for the most accurate classification model from scenario 3 (Fig. 7) was similar to the classified map for the best result from scenario 2, as shown also by the low differences in the user's and producer's accuracies for each class (Table I). However, the classified map for the best result from scenario 1 showed more noise than the maps for the most accurate models from scenarios 2 and 3.

IV. Discussion

A. Effect of Speckle Filtering and Filter Window Size on Classification

The overall accuracies of classification from scenarios 1 and 2 indicate that the application of the speckle filtering in the SAR processing workflow improved the classification results. In both scenarios, the nonfiltered data provided the lowest accuracy, which illustrates that even robust machine learning algorithms, like the random forest, require speckle filtering before the classification of PolSAR data.

The IDAN speckle filter was overall the most effective in producing a highly accurate classification model while the NL-SAR filter produced slightly lower accuracies (the difference in median accuracy was 1% for scenario 1 and 2% for scenario 2). The boxcar filter provided the lowest accuracies of all of the tested speckle filtering methods. The median of the accuracies in both scenarios for the refined Lee and improved Lee sigma methods were equal, however, the refined Lee filter provided the highest accuracies for combinations of small filter windows and large decomposition windows, while the improved Lee sigma filter produced the best models with both processing windows being large.

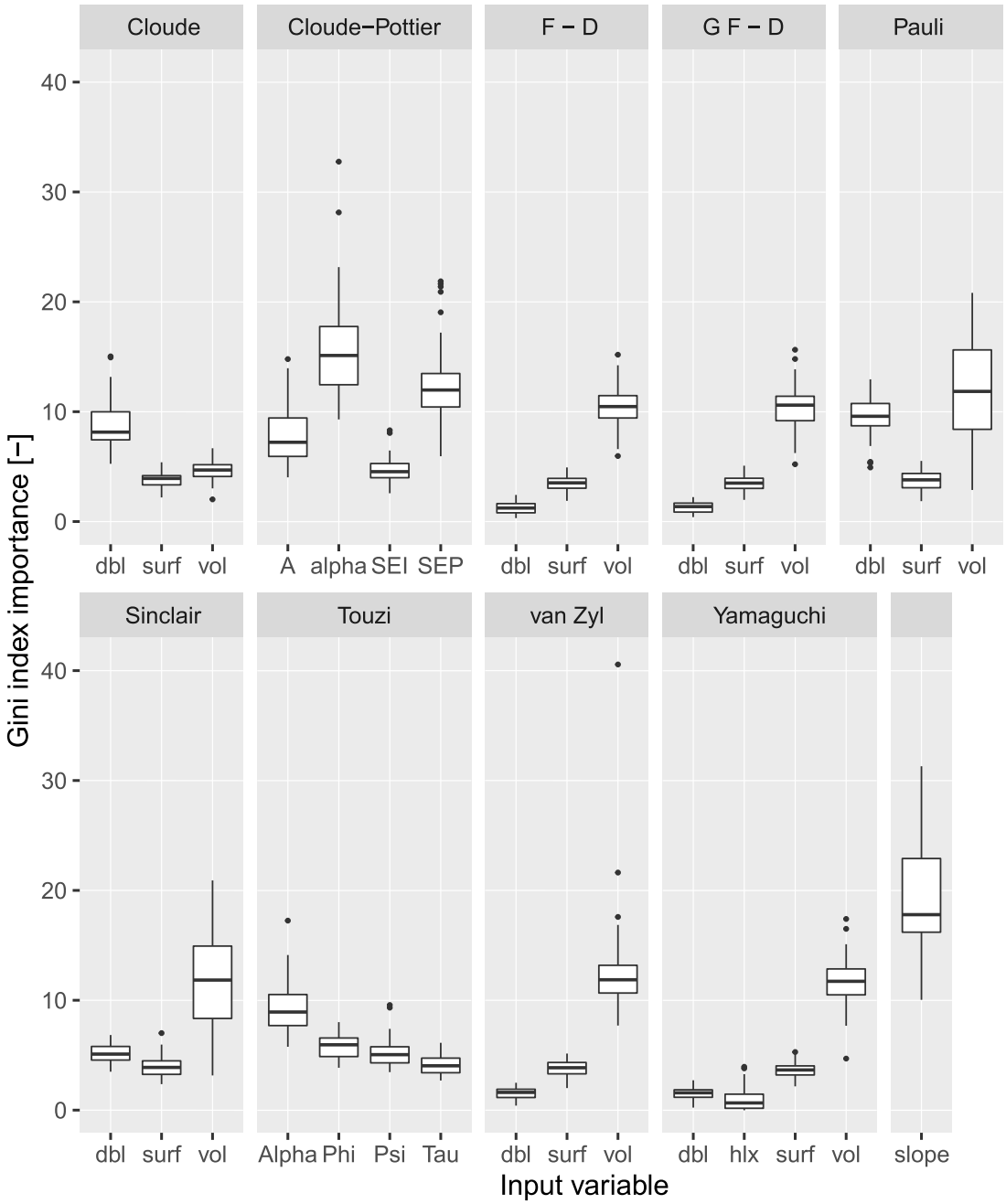

Fig. 5. Box plot of the random forest models predictor importance for each parameter and component of polarimetric decompositions (panel names) in scenario 2. Decomposition abbreviations: Freeman–Durden (F-D), generalized Freeman–Durden (G F-D). The topographic slope (bottom right panel) was not a polarimetric decomposition feature. The higher the Gini index value the predictor is more important.

The comparison of results for data from different sensors (especially between the satellite and airborne or ground-based) may not be reliable. However, the filter mechanics and filter effects on the images are similar no matter the sources of data, which gives some basis for comparison of our research with studies using different sensors. The performance of classification models using different speckle filters in this study is partially in contradiction with the results obtained in a study of land cover classification in South Korea, where the IDAN, refined Lee, and improved Lee sigma methods produced good classification images with similar accuracies, but the highest classification accuracies were achieved by the boxcar filter [12]. The accuracies were therein calculated using a different approach and the data acquired by ground-based SAR was the sub-meter spatial resolution, which may be the cause of the differences in the results. Another research conducted on SAR images of San Francisco also showed results inconsistent with ours, in which the refined Lee filter had better performance than the IDAN based on the Cloude–Pottier decomposition analysis [43]. This was because the study area was much more urbanized than our study, although some vegetation was also present. The refined Lee filter, which preserves well straight edges by selecting

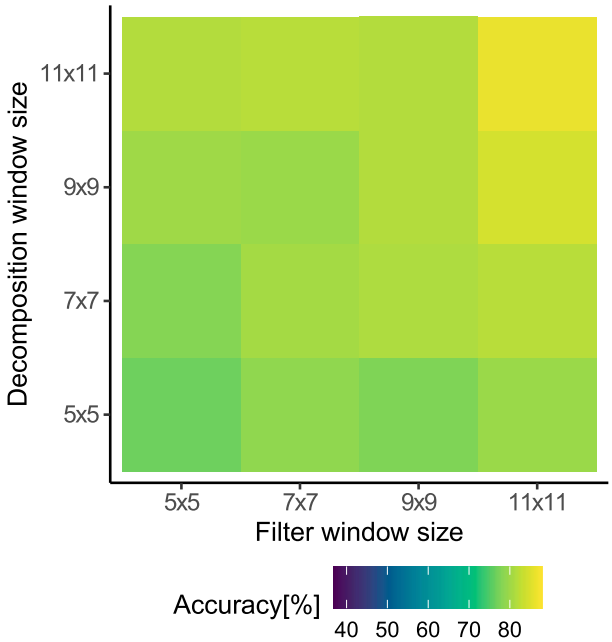

Fig. 6. Accuracy of random forest classification models in scenario 3, where columns show filter window sizes and rows show decomposition window sizes. The accuracy color scale is the same in Figs. 3, 4, and 6.

edge-aligned rectangular windows [28], likely processed better urban area images in that study, because of the presence of features with straight edges.

The results from scenario 2 showed that the impact of the filter window size on the classification accuracy depended on the applied speckle filtering method (Fig. 4). The increase in the size of the filter window for the IDAN method resulted in small changes in the classification accuracies, and each applied window size provided good classification results. This parameter influenced more the improved Lee sigma filter, where the accuracy for the 5×5 window size was 74% and for the best variant (11×11) was 80%.

The highest accuracy for boxcar was achieved by the 9×9 window and for refined Lee by the 7×7 window in scenario 2. The filters applied here were tested and provided similar classification accuracy in a case study in Mumbai, India, which processed C-band (Radarsat 2) and L-band (PALSAR 2) images with a ground resolution of 8 and 24 m, respectively [11]. Additionally, that study investigated the effect of filter windows and recommended minimum windows of 5×5 for the boxcar and 7×7 for the refined Lee algorithms. Another study demonstrated that the most effective method for filtering high-resolution C-band ground-based SAR image (0.7 m in range and from 0.5 to 3.4 m in azimuth) was the refined Lee with a filter window size of 5×5 and 7×7 [12]. However, a study of ALOS-PALSAR urban image classification (spatial resolution 20 m), which processed data only with the refined Lee filter, indicated that the highest classification accuracy was obtained for 3×3 and 5×5 window sizes [14].

The effects of speckle filtering on the results from scenario 2 were also assessed visually by comparison of the Pauli decomposition and classification images (Fig. 8), as a visual inspection is one of the methods used to assess the effectiveness of a filter in smoothing out speckle and preserving image details [22]. Another method for assessment of filtration results is the equivalent number of looks (ENL) metric. The ENL method is reliable for a large, homogeneous area in an SAR image [28]. However, in our case, wetlands are heterogeneous with small vegetation patches and narrow water bodies. Because of that, we decided not to use ENL here.

As shown in the visual comparison, the boxcar filter blurred the image and enlarged strong target signatures [Fig. 8(d)]. For large sliding window sizes, using the boxcar method resulted in losing details and degraded image resolution [Fig. 8(f)]. The refined Lee and boxcar produced a better-filtered image for small windows (5×5, 7×7), which was also shown by Kang [12]. The refined Lee filter preserved single objects well but blurred the river edges for all window sizes [Fig. 8(p) and (r)]. The improved Lee sigma filter showed the most effective performance in maintaining objects' shapes [Fig. 8(l) and (n)]. The river edges were not blurry, and the width of the river was similar to the nonfiltered image. However, the oxbow lake was partially obscured by vegetation. The IDAN filter preserved well the water objects, but it enlarged their surfaces by 2–20 m depending on the window size [Fig. 8(h) and (j)]. In addition, the IDAN filter did not retain small point scatters, such as isolated shrubs. The application of the IDAN and improved Lee sigma filters with large kernel sizes (9×9 or 11×11) smoothed homogeneous areas without blurring the edges as with the boxcar and refined Lee filters. The NL-SAR filter preserved well the river edges and terrain details, similar to the improved Lee sigma filter. In addition, NL-SAR smoothed the homogenous areas comparably to the IDAN and improved Lee sigma filters [Fig. 8(t)].

Effectively, the speckle filters affected the classified object's shape, which was especially visible for linear objects like rivers and oxbow lakes. For large filter windows, the linear objects were preserved only by the IDAN, improved Lee sigma, and NL-SAR filters [Fig. 8(i), (k), (m), (o), and (u)]. The linear objects classified using the boxcar filter were characterized by strong blurring, rounding of edges, and size increase when compared to the other filters [Fig. 8(e)]. The refined Lee method obtained similar results as the improved Lee sigma but only for the 5×5 filter window size [Fig. 8(q)]. The classification with the refined Lee filter with 11×11 filter windows showed a loss of the linear objects, and the objects' boundaries became distorted [Fig. 8(s)]. This was due to the use of the edge-aligned windows in the refined Lee method, which in the case of large filter windows were not suitable for complex edges of natural objects. Overall these results indicate that a better approach to filtering SAR images of natural wetlands was to use pixel-brightness similarities (IDAN, improved Lee sigma) and nonlocal (NL-SAR) than the edge-aligned window (refined Lee) and boxcar filters.

In our case, the use of the NL-SAR filter caused high commission errors of the FVA class to all other classes except SL with the majority of commissions to the DV class. For comparable variants in scenario 2, the user accuracy of FVA class was 62% for NL-SAR and 80% for IDAN in the 5×5 filtration window. As a result, large patches of FVA were present around the river for NL-SAR as opposed to the comparable variants filtered using IDAN or improved Lee sigma (Fig. 8). This indicates that NL-SAR performed too aggressive filtering in our case, which

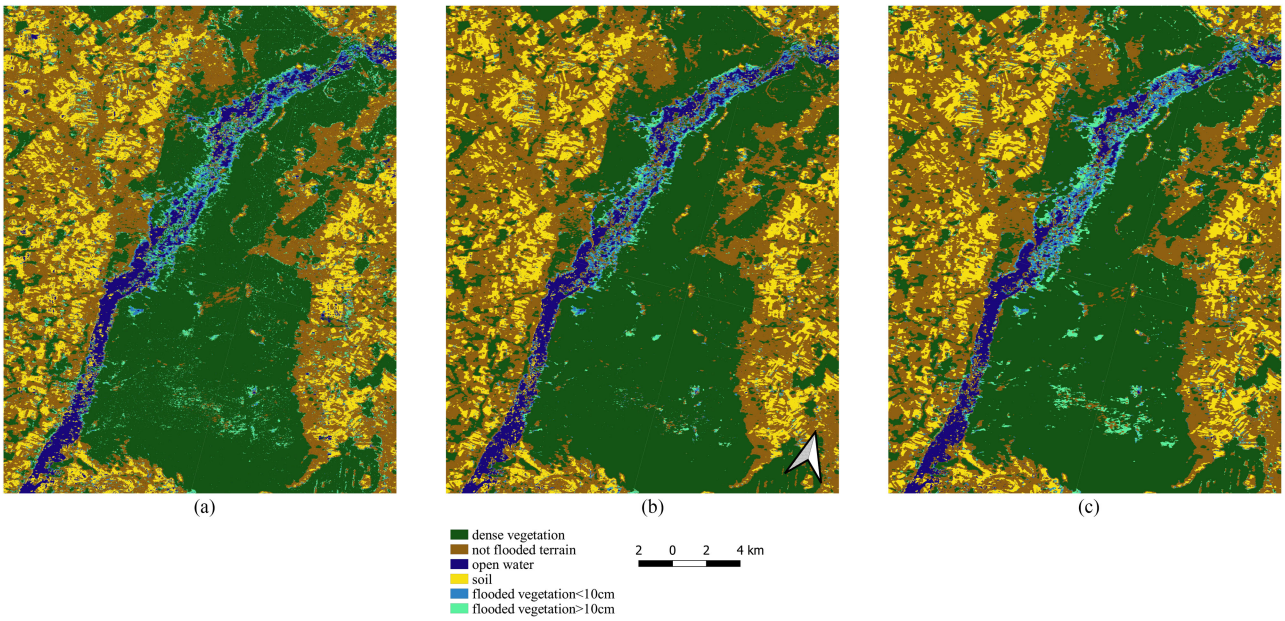

Fig. 7. Classified maps for the most accurate model from scenarios (a) 1, (b) 2, and (c) 3. Corresponding confusion matrices are presented in Table I right column. (a) Scenario 1 Cloude-Pottier in 11×11 window and IDAN in 9×9 window. (b) Scenario 2 all decompositions in 9x9 window and IDAN in 11×11 window. (c) Scenario 3 all filters and decompositions in the 11×11 window.

led to losing polarimetric information related to discrimination of high (>10 cm) vegetation emerging from the water. This issue requires a more detailed analysis, which we leave for future research.

Although the IDAN filter achieved the highest accuracies in scenarios 1 and 2, according to the literature review, it has never been applied before for processing SAR images of inundated river wetlands. The NL-SAR, which gave the best results in the segmentation of watercourses images located in marshes [20], also in our study provided high classification accuracy. The most often used filter in wetlands classification is the refined Lee filter [4], [15] with a 5×5 window [2] or a 7×7 window [5]. Several studies applied the boxcar filter with a 5×5 [7], [16], [17] window size, or the improved Lee sigma filter with a 3×3 [3] or 5×5 [1] window. This shows the underestimation of the IDAN and NL-SAR filters in research, which may be due to the lack of an easy-to-use implementation until recently.

B. Effect of Polarimetric Decomposition on Classification in Scenario 1

Overall, scenario 1 indicated that the Cloude–Pottier decomposition, regardless of the filter used and the size of the processing windows, provided the highest classification accuracies. The model-based decompositions (Freeman–Durden, Generalized Freeman–Durden, and Yamaguchi) and van Zyl (based on eigenvectors, but may be considered as model-based [2]) obtained similar classification accuracies (for the same decomposition or filtering window size variants) which were always lower than the Cloude–Pottier. The high classification accuracy in the Cloude–Pottier decomposition is confirmed by another study that distinguished similar classes [4]. Conversely, other studies using X- and S-band airborne data [3] or conducted for wetlands in the full vegetative stage [1], [2] showed that applying the Cloude–Pottier decomposition was less successful when compared to model-based decompositions.

The lowest accuracy in scenario 1 was achieved by the Touzi decomposition. It was caused by its helicity and orientation components, which had relatively low importance in our study. Yet, the alpha angle showed clear spatial patterns of the scattering mechanisms. Similarly, a study of the efficiency of various SAR features and decomposition methods for discriminating wetland classes in Canada did not recommend using the Touzi decomposition for wetland classification due to its noisy results [44]. Conversely, other studies demonstrated that the Touzi decomposition allows for accurate wetlands classification when a different methodology is applied. A study in the Canadian wetland showed that using the Touzi decomposition data produces higher classification accuracy than Cloude–Pottier and Freeman–Durden decompositions (each scenario used SAR intensities as additional input data) [45]. Yet that study, was conducted in bog-dominated wetlands, which are characterized by sphagnum vegetation that is different from fen vegetation present in the Biebrza basin.

C. Importance of Polarimetric Predictors in Scenario 2 Classification Models

The highest values of the polarimetric predictors' importance achieved the alpha parameter and polarimetric contribution of the Shannon entropy from the Cloude–Pottier decomposition. On contrary, another study showed that Shannon entropy and intensity contribution of Shannon entropy were the most discriminating predictors, while the polarimetric contribution of Shannon entropy and the alpha parameter were the least discriminating predictors for grassland classification [5].

For the model-based polarimetric decompositions, the volume components were the most important scattering mechanism.

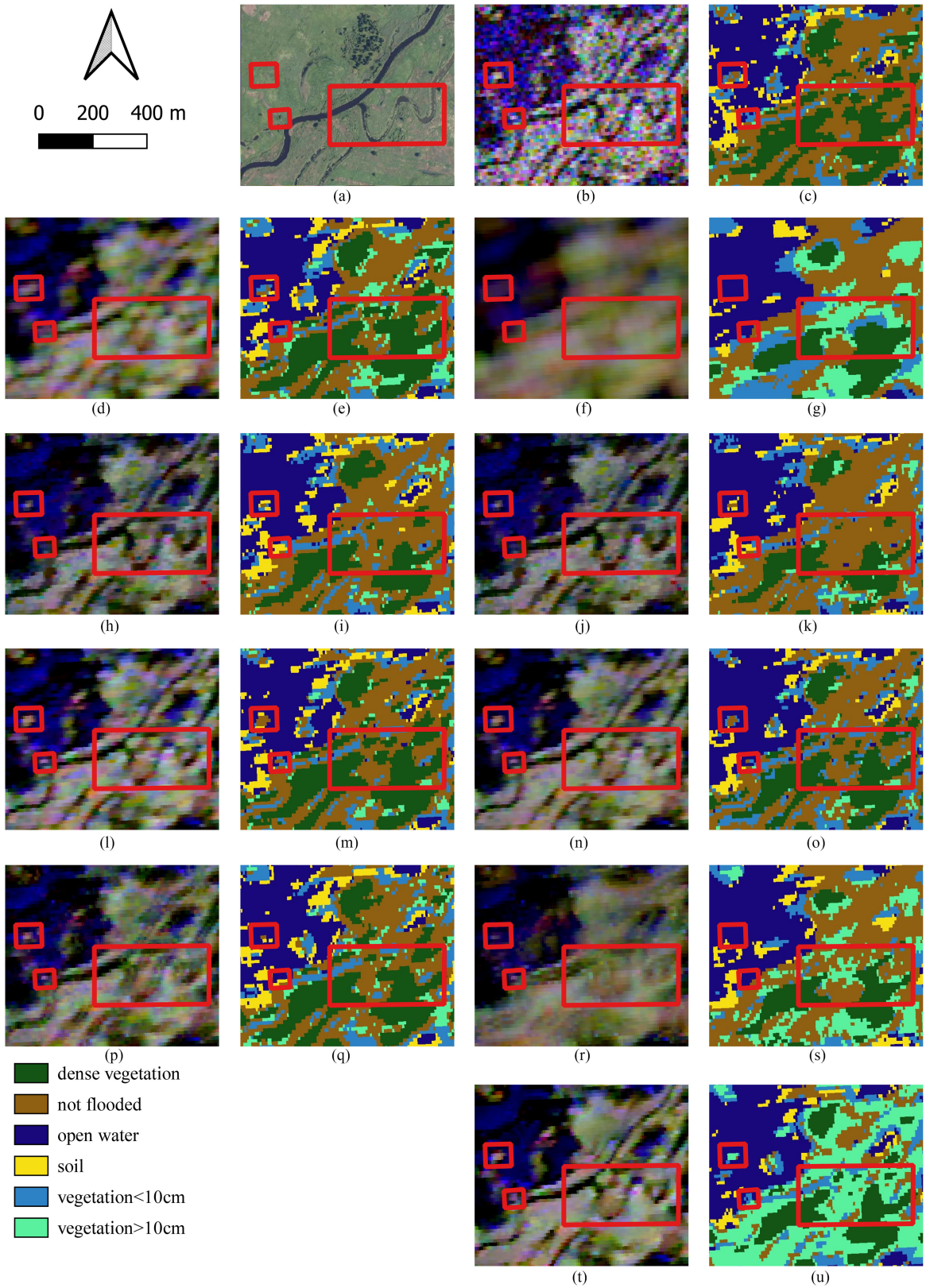

Fig. 8. Comparison of the speckle filtering effect and resulting classification, for various terrain objects, in the Pauli decomposition and classification images with a 5×5 decomposition window size from scenario 2. The selected objects in the compared images are shrubs, tussocks, and a river with an oxbow lake, indicated with the small, medium, and large red boxes, respectively. The orthophoto map (panel a) was acquired before flooding, therefore, no flooding extent is visible. (a) ortophoto. (b) non-filtered. (c) non-filtered. (d) boxcar 5×5. (e) boxcar 5×5. (f) boxcar 11×11. (g) boxcar 11×11. (h) IDAN 5×5. (i) IDAN 5×5. (j) IDAN 11×11. (k) IDAN 11×11. (l) improved Lee sigma 5×5. (m) improved Lee sigma 5×5. (n) improved Lee sigma 11×11. (o) improved Lee sigma 11×11. (p) refined Lee 5×5. (q) refined Lee 5×5. (r) refined Lee 11×11. (s) refined Lee 11×11. (t) NL-SAR. (u) NL-SAR.

This was because volume scattering is the dominant scattering mechanism over vegetation canopies. The surface and double scattering components had considerably lower importance. This is counterintuitive because one would expect that the presence of water (surface scattering) [46] and an emergent vegetation boundary (double scattering) [16] are good indicators of the presence of flooding. Overall, it was more important for the random forest models to identify the volume scattering than the surface or double scattering to assign a proper classification label. Similar results were presented in another study that used satellite data from the same sensor with a close acquisition date [5].

The volume components from Pauli and Sinclair decompositions had similar, high importance when compared to the volume components from model-based decompositions. Another interesting feature was the double scattering component, which was important for the Cloude and Pauli decomposition and not important for the model-based decompositions. This suggests that the model-based decompositions identified a lesser contribution of volume (e.g., vegetation paths) and double scattering (e.g., present at the boundary of open water and vegetation) mechanisms in this study area.

The helix component from the Yamaguchi decomposition, which was considered less relevant in a natural environment [34] had the lowest importance for our study area. This component was evaluated as useless for wetland classification in other studies using quad-pol Radarsat-2 data [5], [44]. On the other hand, for PALSAR 2 data, the helix component improved the classification accuracy [4], which may be due to the longer wavelength of the L-band used in that study than the C-band used here.

The alpha component from Touzi decomposition was one of the most important parameters in the classification model, which was also confirmed in another study [44]. This component defines the dominant scattering mechanism alike the Cloude–Pottier alpha parameter, therefore, it may be important for our study area due to the presence of different scattering mechanisms in the mosaic of inundation, emergent, and dense vegetation in the Biebrza wetlands. Importantly, temporal changes in the alpha component and other Touzi decomposition parameters can be used to discriminate between different wetland vegetation types [47]. Yet, in another study, the phase parameter from Touzi decomposition was considered an important variable due to the ability to discriminate between fen and bog wetlands [26]. However, our results did not show this effect because the lower Biebrza wetland is dominated by fen wetlands without bog vegetation.

D. Effect of Decomposition Window Size on Classification Accuracy

The increase in the size of the decomposition window resulted in the improvement of the overall accuracy obtained with eigenvectors-based decompositions, such as Cloude, Cloude–Pottier, and Touzi. Conversely, the results for the model-based decompositions (Freeman–Durden, generalized Freeman–Durden, van Zyl, and Yamaguchi) had higher classification accuracies for smaller decomposition windows (5×5, 7×7). According to the previous study [14], these results confirm that there is no single, optimal decomposition window size for all polarimetric decompositions. However, we identified is some relations between groups of decompositions and the decomposition window sizes. A large decomposition window was more suitable for eigenvector-based decompositions, and a smaller one for model-based decompositions. We believe this is due to the eigenvector-based decompositions estimate the main backscattering mechanism using an angular component (the alpha component in Cloude–Pottier and Touzi), which may need a larger decomposition window to decrease noise than the intensity components of each scattering mechanism in the model-based decompositions.

Our study demonstrated that the decomposition window size impacts classification accuracy, which was previously shown for cases when decomposition windows were larger than the filter windows [14]. We summarized the results from scenario 1 (Fig. 3) to see how many times the classification accuracy for a decomposition window size smaller than the filter window size will be higher than 5% (which is approx. the 95% confidence interval size for our classification accuracy) given the same decomposition and filter method. The classification accuracies were higher seven out of 54 times for the IDAN, and seven out of 54 times for the improved Lee sigma filter. The boxcar and the refined Lee filter accuracies were never higher than 5% in this analysis. Therefore, the decomposition window size is an important parameter when using filters that properly preserve the object shape, i.e., IDAN, and improved Lee sigma. For these filters, the application of a decomposition window smaller than the filter window can improve the classification accuracy when compared to variants with the decomposition window size the same or larger than the filter window size. The NL-SAR was not tested in this analysis due to too few cases resulting from different parametrizations than local filters. However, we expect the NL-SAR filter will show similar behavior as IDAN, and improved Lee sigma filters.

E. Entire Dataset Classification in Scenario 3

The aim of scenario 3 was to verify if the use of all decomposition products processed with various speckle filters on the classification input would improve the classification accuracy. The difference between the highest accuracies from scenarios 1 and 3 was 14%, which is a considerable improvement. However, only two combinations of processing windows in scenario 3 achieved higher accuracy than the best result from scenario 2. The accuracy gain in scenario 3 was 1.8% when compared to scenario 2. This is a rather small improvement, especially given that the preparation of the input dataset and creating a random forest model for one variant in scenario 3 (2.5 h) takes four times longer than for one variant in scenario 2 (0.6 h).

In scenario 2, the inclusion of multiple decomposition data allowed for better discrimination of FVA from DV and NFT classes. The most of misclassifications in the best scenario 2 occurred between OW, SL, and FVB classes. These misclassifications were increased in the best model of scenario 3, which used multiple decompositions and multiple filtering data. Hence, although scenario 3 increased overall accuracy in reference to

scenario 2 the difficult classes decreased their user and producer accuracy. This may be a result of fitting to noise, which is an undesired behavior of classification models with a large number of predictors.

F. Sensitivity of Accuracy to Processing Window Size

The values of the sensitivity analysis for the IDAN filter were about ten times higher for the decomposition window than for the filter window. This means that the decomposition window size influences the classification accuracy more than the filter window size, and is an important parameter for the IDAN filter. The same applies to the results of the refined Lee, improved Lee sigma, and NL-SAR filters.

In the case of the boxcar filter, both filter and decomposition windows had a similar, low impact on accuracy. This is because the boxcar filter and the averaging in the decomposition window finally produce the same effect.

As expected, the decomposition window size was an important parameter for the nonfiltered coherency matrix because increasing the decomposition window size caused an increasing averaging of input data and decreased the noise.

The sensitivity analysis from scenario 3 demonstrated that the decomposition window had a slightly greater impact on the classification accuracy than the filter window. This could be due to mixing different filter methods, which produced an antagonistic effect on the sensitivities, effectively producing similar s_f and s_d figures.

G. Outlook

In our study, we used several well-established filters and the NL-SAR filter, which belongs to a group of relatively novel and promising nonlocal speckle filters. The NL-SAR filter showed good filtering performances for wetland classification, therefore, in future research, other nonlocal filters should be tested. Another promising method is the SimiTest, which is based on the similarity test for complex Wishart distributed covariance matrices, using polarimetric and interferometric information [48]. SimiTest showed that it smoothed speckle in the homogenous area and preserved the details better than the boxcar and refined Lee filters. Also, the extension of this method, named CCM+SimiTest, which proposed the new context covariance matrix formulation and a fast similarity test computation scheme, achieved more satisfying performance on speckle reduction and details preservation than local and nonlocal filters [49]. Yet another approach, is to use the coefficient of variance and Pauli basis (CVPB-NLM) to measure the similarity, which showed higher ENL metrics than the refined Lee filter [50].

Except for the polarimetric decomposition methods described in this study, some recently developed methods require testing in wetlands classification. One of such methods could be the general double- and odd-bounce scattering models with independent orientation angles, which improved the discrimination of the built-up patches from the forest areas [51]. Other interesting approaches focus directly on polarimetric parameters, such as the oscillation amplitudes and oscillation centers of each element of a coherency matrix, which yielded good performance for man-made target characterization [52], or the null angle parameters, which were sensitive to crop types and produced high classification accuracy even with very limited training samples [53].

Unfortunately, the limitation of incorporation of new methodologies in PolSAR studies is low reproducibility. Most of the recently proposed methods are lacking accessible source code or software implementation. Own implementation of models and algorithms is possible, however, requires additional resources and testing.

V. Conclusion

In this study, the Radarsat 2 image of a fen wetland in northeast Poland was classified in multiple scenarios to test the effect of the following polarimetric methods and their processing parameters on the classification accuracy.

1) *Five Speckle Filters*: boxcar, IDAN, improved Lee sigma, refined Lee, and NL-SAR, and a nonfiltered coherency matrix.
2) *Four Filter Window Sizes*: 5×5, 7×7, 9×9, and 11×11 (except the nonlocal NL-SAR filter).
3) *Nine Polarimetric Decompositions*: Cloude, Cloude–Pottier, Freeman–Durden, generalized Freeman–Durden, Pauli, Sinclair, van Zyl, and Yamaguchi.
4) *Four Decomposition Window Sizes*: 5×5, 7×7, 9×9, and 11×11.

Further, the data were used as an input in random forest classification models that discriminated six land cover classes in a flooded wetland environment. The data were classified in single- and multidecomposition scenarios. We aimed to demonstrate the impact of processing parameters on classification accuracy, to find the best combination of processing parameters and the most suitable polarimetric decomposition for wetland mapping.

Our results show that the selection of the processing parameters significantly influences classification accuracy. Scenario 1 (single decomposition) and scenario 2 (multiple decompositions with the same speckle filter) showed that the IDAN filter with an 11×11 filter window size and a 9×9 decomposition window size provided the highest classification accuracy. However, the selection of the filtering method and the window size has to take into account the expected degree of detail preservation. If single- or few-pixel scatters (e.g., shrub, tree) are present in the study area, and should be preserved, we recommend using the refined Lee or improved Lee sigma with small filtering windows. Such parametrization may result in insufficient speckle removal within the homogeneous areas, and the introduction of single misclassified pixels. When the aim is to smooth the homogeneous areas and preserve the edges of the objects without retaining small terrain details, the best results are obtained when using the IDAN and improved Lee sigma filters with a large window. In our study, the nonlocal NL-SAR filter retained well the small terrain objects and resulted in a strong smoothing for homogenous areas, which effectively led to some misclassifications of inundated vegetation.

This research showed that classification models using polarimetric features from multiple decompositions (scenarios 2 and 3) usually provide higher accuracy than the classification

models using components or parameters from one polarimetric decomposition. The exception was the Cloude–Pottier decomposition, which had the highest overall accuracy in scenario 1, and had higher accuracy than several variants from scenario 2. The predictors' importance of the classification models demonstrated that the Cloude–Pottier decomposition components and the volume components from the Yamaguchi, Pauli, Sinclair, and van Zyl decompositions were the most important parameters for wetland classification in this study.

Our study showed that the decomposition window has a different effect on model-based and eigenvector-based decompositions. We suggest using a smaller (5×5, 7×7) decomposition window for model-based, and a larger (9×9, 11×11) for eigenvector-based decomposition. We suggest processing the SAR data with a decomposition window size smaller than the filter window size for filters, which preserves the object' s shape well (IDAN, and improved Lee sigma).

Overall, based on the accuracy of all scenarios, we recommend performing classification with the Cloude–Pottier, van Zyl, Yamaguchi, and Pauli decompositions processed with the IDAN speckle filter.

Finally, the vegetation of wetlands around the world is very diverse, so our conclusions are representative for comparable fen wetlands of the temperate climate zone. An analogous study conducted in a different study area would be desired to support our result. Apart from that, future research should extend the methods to speckle filters and polarimetric decomposition described in the outlook section, different SAR bands, especially longer wavelengths, and different spatial resolutions.

Acknowledgment

The field sampling was conducted in the Biebrza National Park, Poland under an appropriate permit. LiDAR DEM was provided by Biebrza National Park, the Orthophoto map was provided by the WMS service of the Head Office of Geodesy and Cartography (GUGiK) in Poland. Landsat data were provided by NASA-USGS.

References

[1] M. Mahdianpari, B. Salehi, F. Mohammadimanesh, and M. Motagh, "Random forest wetland classification using ALOS-2 L-band, RADARSAT-2 C-band, and TerraSAR-X imagery," *ISPRS J. Photogramm. Remote Sens.*, vol. 130, pp. 13–31, Aug. 2017.

[2] L. F. de Almeida Furtado, T. S. F. Silva, and E. M. L. de MoraesNovo, "Dual-season and full-polarimetric C band SAR assessment for vegetation mapping in the Amazon várzea wetlands," *Remote Sens. Environ.*, vol. 174, pp. 212–222, Mar. 2016.

[3] S. van Beijma, A. Comber, and A. Lamb, "Random forest classification of salt marsh vegetation habitats using quad-polarimetric airborne SAR, elevation and optical RS data," *Remote Sens. Environ.*, vol. 149, pp. 118–129, Jun. 2014.

[4] S. Plank, M. Jüssi, S. Martinis, and A. Twele, "Mapping of flooded vegetation by means of polarimetric Sentinel-1 and ALOS-2/PALSAR-2 imagery," *Int. J. Remote Sens.*, vol. 38, no. 13, pp. 3831–3850, Mar. 2017.

[5] S. Rapinel, J. Betbeder, J. Denize, E. Fabre, É. Pottier, and L. Hubert-Moy, "SAR analysis of wetland ecosystems: Effects of band frequency, polarization mode and acquisition dates," *ISPRS J. Photogramm. Remote Sens.*, vol. 170, pp. 103–113, Dec. 2020.

[6] N. Morandeira, F. Grings, C. Facchinetti, and P. Kandus, "Mapping plant functional types in floodplain wetlands: An analysis of C-band polarimetric SAR data from RADARSAT-2," *Remote Sens.*, vol. 8, no. 3, Feb. 2016, Art. no. 174.

[7] L. White, B. Brisco, M. Dabboor, A. Schmitt, and A. Pratt, "A collection of SAR methodologies for monitoring wetlands," *Remote Sens.*, vol. 7, no. 6, pp. 7615–7645, Jun. 2015.

[8] J.-S. Lee, T. L. Ainsworth, J. P. Kelly, and C. Lopez-Martinez, "Evaluation and bias removal of multilook effect on entropy/alpha/anisotropy in polarimetric SAR decomposition," *IEEE Trans. Geosci. Remote Sens.*, vol. 46, no. 10, pp. 3039–3052, Oct. 2008.

[9] S. Foucher and C. Lopez-Martinez, "Analysis, evaluation, and comparison of polarimetric SAR speckle filtering techniques," *IEEE Trans. Image Process.*, vol. 23, no. 4, pp. 1751–1764, Apr. 2014.

[10] J.-S. Lee, M. Grunes, and G. de Grandi, "Polarimetric SAR speckle filtering and its implication for classification," *IEEE Trans. Geosci. Remote Sens.*, vol. 37, no. 5, pp. 2363–2373, Sep. 1999.

[11] S. Shitole, S. De, Y. S. Rao, B. K. Mohan, and A. Das, "Selection of suitable window size for speckle reduction and deblurring using SOFM in polarimetric SAR images," *J. Indian Soc. Remote Sens.*, vol. 43, no. 4, pp. 739–750, Jul. 2015.

[12] M.-K. Kang, K.-E. Kim, S.-J. Cho, H. Lee, and J.-H. Lee, "Filtering effect in supervised classification of polarimetric ground based SAR images," *Korean J. Remote Sens.*, vol. 26, no. 6, pp. 705–719, Dec. 2010.

[13] L. D. Robertson *et al.*, "Synthetic aperture radar (SAR) image processing for operational space-based agriculture mapping," *Int. J. Remote Sens.*, vol. 41, no. 18, pp. 7112–7144, Jun. 2020.

[14] E. Woźniak, W. Kofman, P. Wajer, S. Lewiński, and A. Nowakowski, "The influence of filtration and decomposition window size on the threshold value and accuracy of land-cover classification of polarimetric SAR images," *Int. J. Remote Sens.*, vol. 37, no. 1, pp. 212–228, Dec. 2015.

[15] Y. T. Jung, S.-E. Park, C.-S. Baek, and D.-H. Kim, "Evaluation of polarimetric parameters for flood detection using PALSAR-2 quad-pol data," *Korean J. Remote Sens.*, vol. 34, no. 1, pp. 117–126, Feb. 2018.

[16] B. Brisco *et al.*, "Polarimetric decompositions of temperate wetlands at C-band," *IEEE J. Sel. Topics Appl. Earth Observ. Remote Sens.*, vol. 8, no. 7, pp. 3585–3594, Jul. 2015.

[17] F. Mohammadimanesh, B. Salehi, M. Mahdianpari, B. Brisco, and E. Gill, "Full and simulated compact polarimetry SAR responses to canadian wetlands: Separability analysis and classification," *Remote Sens.*, vol. 11, no. 5, Mar. 2019, Art. no. 516.

[18] E. Ferrentino, A. Buono, F. Nunziata, A. Marino, and M. Migliaccio, "On the use of multipolarization satellite SAR data for coastline extraction in harsh coastal environments: The case of Solway Firth," *IEEE J. Sel. Topics Appl. Earth Observ. Remote Sens.*, vol. 14, pp. 249–257, 2021.

[19] M. Schmitt, G. Baier, and X. X. Zhu, "Potential of nonlocally filtered pursuit monostatic TanDEM-X data for coastline detection," *ISPRS J. Photogramm. Remote Sens.*, vol. 148, pp. 130–141, Feb. 2019.

[20] N. S. Morandeira, R. Grimson, and P. Kandus, "Assessment of SAR speckle filters in the context of object-based image analysis," *Remote Sens. Lett.*, vol. 7, no. 2, pp. 150–159, Dec. 2015.

[21] S. P. S. Kushwaha, R. S. Dwivedi, and B. R. M. Rao, "Evaluation of various digital image processing techniques for detection of coastal wetlands using ERS-1 SAR data," *Int. J. Remote Sens.*, vol. 21, no. 3, pp. 565–579, Jan. 2000.

[22] V. K. Rana and T. Suryanarayana, "Evaluation of SAR speckle filter technique for inundation mapping," *Remote Sens. Appl. Soc. Environ.*, vol. 16, Nov. 2019, Art. no. 100271.

[23] M. Mahdianpari, B. Salehi, and F. Mohammadimanesh, "The effect of PolSAR image de-speckling on wetland classification: Introducing a new adaptive method," *Can. J. Remote Sens.*, vol. 43, no. 5, pp. 485–503, Sep. 2017.

[24] C. Marechal, E. Pottier, L. Hubert-Moy, and S. Rapinel, "One year wetland survey investigations from quad-pol RADARSAT-2 time-series SAR images," *Can. J. Remote Sens.*, vol. 38, no. 3, pp. 240–252, 2012.

[25] B. Brisco, M. Kapfer, T. Hirose, B. Tedford, and J. Liu, "Evaluation of C-band polarization diversity and polarimetry for wetland mapping," *Can. J. Remote Sens.*, vol. 37, no. 1, pp. 82–92, 2011.

[26] R. Touzi, A. Deschamps, and G. Rother, "Phase of target scattering for wetland characterization using polarimetric C-band SAR," *IEEE Trans. Geosci. Remote Sens.*, vol. 47, no. 9, pp. 3241–3261, Sep. 2009.

[27] J. S. Lee, L. Jurkevich, P. Dewaele, P. Wambacq, and A. Oosterlinck, "Speckle filtering of synthetic aperture radar images: A review," *Remote Sens. Rev.*, vol. 8, no. 4, pp. 313–340, Feb. 1994.

[28] J.-S. Lee and E. Pottier, *Polarimetric Radar Imaging*, J.-S. Lee and E. Pottier, Eds. Boca Raton, FL, USA: CRC Press, 2017.

[29] G. Vasile, E. Trouve, J.-S. Lee, and V. Buzuloiu, "Intensity-driven adaptive-neighborhood technique for polarimetric and interferometric SAR parameters estimation," *IEEE Trans. Geosci. Remote Sens.*, vol. 44, no. 6, pp. 1609–1621, Jun. 2006.

[30] J.-S. Lee, T. L. Ainsworth, Y. Wang, and K.-S. Chen, "Polarimetric SAR speckle filtering and the extended sigma filter," *IEEE Trans. Geosci. Remote Sens.*, vol. 53, no. 3, pp. 1150–1160, Mar. 2015.
[31] C.-A. Deledalle, L. Denis, F. Tupin, A. Reigber, and M. Jager, "NL-SAR: A unified nonlocal framework for resolution-preserving (Pol) (In)SAR denoising," *IEEE Trans. Geosci. Remote Sens.*, vol. 53, no. 4, pp. 2021–2038, Apr. 2015.
[32] S.-W. Chen, X.-C. Cui, X.-S. Wang, and S.-P. Xiao, "Speckle-free SAR image ship detection," *IEEE Trans. Image Process.*, vol. 30, pp. 5969–5983, 2021.
[33] A. Freeman and S. Durden, "A three-component scattering model for polarimetric SAR data," *IEEE Trans. Geosci. Remote Sens.*, vol. 36, no. 3, pp. 963–973, May 1998.
[34] Y. Yamaguchi, T. Moriyama, M. Ishido, and H. Yamada, "Four-component scattering model for polarimetric SAR image decomposition," *IEEE Trans. Geosci. Remote Sens.*, vol. 43, no. 8, pp. 1699–1706, Aug. 2005.
[35] P. Réfrégier and J. Morio, "Shannon entropy of partially polarized and partially coherent light with Gaussian fluctuations," *J. Opt. Soc. Amer. A*, vol. 23, no. 12, Dec. 2006, Art. no. 3036.
[36] T. Berezowski, M. Gierszewska, and T. Bielinski, "Flood classification in a natural wetland for early spring conditions using various polarimetric SAR methods," in *Proc. IEEE Int. Geosci. Remote Sens. Symp.*, 2021, pp. 6853–6856.
[37] T. Berezowski, D. Partington, J. Chormański, and O. Batelaan, "Spatiotemporal dynamics of the active perirheic zone in a natural wetland floodplain," *Water Resour. Res.*, vol. 55, no. 11, pp. 9544–9562, Nov. 2019.
[38] M. J. Wassen *et al.*, "Eco-hydrological functioning of the Biebrza wetlands: Lessons for the conservation and restoration of deteriorated wetlands," in *Wetlands: Functioning, Biodiversity Conservation, and Restoration*. Berlin, Germany: Springer, 2006, pp. 285–310.
[39] M. Belgiu and L. Drăguţ, "Random forest in remote sensing: A review of applications and future directions," *ISPRS J. Photogramm. Remote Sens.*, vol. 114, pp. 24–31, Apr. 2016.
[40] L. Breiman, "Random forests," *Mach. Learn.*, vol. 45, no. 1, pp. 5–32, 2001.
[41] W. H. Kruskal and W. A. Wallis, "Use of ranks in one-criterion variance analysis," *J. Amer. Stat. Assoc.*, vol. 47, no. 260, pp. 583–621, 1952.
[42] O. J. Dunn, "Multiple comparisons using rank sums," *Technometrics*, vol. 6, no. 3, pp. 241–252, 1964. [Online]. Available: https://www.tandfonline.com/doi/abs/10.1080/00401706.1964.10490181
[43] F. Cao *et al.*, "Influence of speckle filtering of polarimetric SAR data on different classification methods," in *Proc. IEEE Int. Geosci. Remote Sens. Symp.*, 2011, pp. 1052–1055.
[44] M. Amani, B. Salehi, S. Mahdavi, and B. Brisco, "Separability analysis of wetlands in Canada using multi-source SAR data," *GISci. Remote Sens.*, vol. 56, no. 8, pp. 1233–1260, Jul. 2019.
[45] K. Millard and M. Richardson, "Wetland mapping with LiDAR derivatives, SAR polarimetric decompositions, and LiDAR-SAR fusion using a random forest classifier," *Can. J. Remote Sens.*, vol. 39, no. 4, pp. 290–307, 2013. [Online]. Available: https://doi.org/10.5589/m13-038
[46] S. Mahdavi, B. Salehi, J. Granger, M. Amani, B. Brisco, and W. Huang, "Remote sensing for wetland classification: A comprehensive review," *GISci. Remote Sens.*, vol. 55, no. 5, pp. 623–658, Dec. 2017.
[47] G. Gosselin, R. Touzi, and F. Cavayas, "Polarimetric Radarsat-2 wetland classification using the Touzi decomposition: Case of the Lac Saint-Pierre Ramsar wetland," *Can. J. Remote Sens.*, vol. 39, no. 6, pp. 491–506, 2014. [Online]. Available: https://doi.org/10.5589/m14-002
[48] S.-W. Chen, X.-S. Wang, and M. Sato, "PolInSAR complex coherence estimation based on covariance matrix similarity test," *IEEE Trans. Geosci. Remote Sens.*, vol. 50, no. 11, pp. 4699–4710, Nov. 2012.
[49] S.-W. Chen, "SAR image speckle filtering with context covariance matrix formulation and similarity test," *IEEE Trans. Image Process.*, vol. 29, pp. 6641–6654, 2020.
[50] X. Xing, Q. Chen, S. Yang, and X. Liu, "Feature-based nonlocal polarimetric SAR filtering," *Remote Sens.*, vol. 9, no. 10, Oct. 2017, Art. no. 1043.
[51] S.-W. Chen and M. Sato, "General polarimetric model-based decomposition for coherency matrix," in *Proc. IEEE Int. Geosci. Remote Sens. Symp.*, 2012, pp. 1843–1855.
[52] S.-W. Chen, X.-S. Wang, and M. Sato, "Uniform polarimetric matrix rotation theory and its applications," *IEEE Trans. Geosci. Remote Sens.*, vol. 52, no. 8, pp. 4756–4770, Aug. 2014.
[53] S.-W. Chen and C.-S. Tao, "PolSAR image classification using polarimetric-feature-driven deep convolutional neural network," *IEEE Geosci. Remote Sens. Lett.*, vol. 15, no. 4, pp. 627–631, Apr. 2018.

Monika Gierszewska was born in Człuchów, Poland, in 1996. She received the B.S. degree in geodesy and cartography and the M.S degree in space and satellite technologies in 2018 and 2019, respectively, from the Gdańsk University of Technology, Gdańsk, Poland.

Since 2020, she has been working on her Ph.D. dissertation on flooded areas detection on SAR images with an application of different machine learning and deep learning methods with the Department of Geoinformatics from Gdańsk University of Technology, Gdańsk, Poland.

Her research interests include remote sensing, particularly the polarimetric SAR data analysis in mapping the extent of floods and flooded vegetation.

Tomasz Berezowski (Member, IEEE) was born in Warsaw, Poland, in 1986. He received the B.S. and M.S. degrees in environmental protection from the Warsaw University of Life Sciences, Warsaw, Poland, in 2010, and the Ph.D. degree in engineering from Vrije Universiteit, Brussel, Belgium, in 2015.

From 2014 to 2017, he was with the Department of Hydrology and Water Resources, Warsaw University of Life Sciences. Since 2017, he has been an Assistant Professor with the Department of Geoinformatics, Gdańsk University of Technology, Gdańsk, Poland. From 2014 and 2015, he was a Visiting Scholar with Flinders University, Bedford Park, SA, Australia. He has authored 18 JCR publications. His research interests include applications of remote sensing in hydrology, especially in hydrological modeling.